Visual Neuroscience

ARTICLE

Open Access

https://doi.org/10.48130/vns-0026-0046

Visual Neuroscience **2026**, 43: e048

Kurarinone as a potential therapeutic agent targeting the retinal neurovascular unit in ischemic conditions

Yunhong Shi[1,2#], Naiyuan Zhang[3#], Yulin Zhuo[4#], Yuqiao Liao[2#], Chenyu Ma[2], Yiji Pan[2], Yuhan Luo[2], Siwen Zang[2], Xinran Dong[2], Cheng Yang[2], Yong Wang[2], Zhixing Cheng[2], Zhaohao Huang[2*], Wenru Su[5*] and Honghua Yu[1*]

[1] *Joint Shantou International Eye Center of Shantou University and The Chinese University of Hong Kong, Shantou 515000, China*

[2] *Guangdong Eye Institute, Department of Ophthalmology, Guangdong Provincial People's Hospital (Guangdong Academy of Medical Sciences), Southern Medical University, Guangzhou 510080, China*

[3] *Department of Ophthalmology, Beijing Institute of Ophthalmology, Beijing Tongren Hospital, Capital Medical University, Beijing 100041, China*

[4] *School of Optometry, The Hong Kong Polytechnic University, Hong Kong 999077, China*

[5] *Department of Ophthalmology, Shanghai Key Laboratory of Orbital Diseases and Ocular Oncology, Shanghai Ninth People's Hospital, Shanghai Jiao Tong University School of Medicine, Shanghai 200011, China*

[#] Authors contributed equally: Yunhong Shi, Naiyuan Zhang, Yulin Zhuo, Yuqiao Liao

[*] Correspondence: ZOChuangzhaohao@163.com (Huang Z); suwr3@mail.sysu.edu.cn (Su W); yuhonghua@stu.edu.cn (Yu H)

Abstract

Neuroinflammation and ferroptosis contribute to retinal ganglion cell (RGC) degeneration in glaucoma. Kurarinone (KU), a bioactive flavanone from *Sophora flavescens*, has anti-inflammatory properties, but its neuroprotective role in retinal ischemia remains unclear. A mouse model of acute ocular hypertension-induced retinal ischemia-reperfusion (RIR) injury was used to assess KU pretreatment on retinal structure, RGC survival, glial activation, oxidative stress, mitochondrial morphology, and iron homeostasis. Single-cell RNA sequencing identified candidate transcriptional programs. Oxygen-glucose deprivation/reoxygenation (OGD/R)-challenged BV-2 microglia were used for mechanistic experiments with pharmacological modulation of STING and LCN2. KU preserved retinal architecture, reduced RGC loss and cell death, and attenuated oxidative stress and glial activation after RIR. Single-cell analysis identified inflammatory- and ferroptosis-related transcriptional programs, particularly in microglia, that were altered in KU-treated retinas. In OGD/R-treated microglia, KU reduced reactive oxygen species and intracellular Fe^{2+} accumulation, increased FPN and GPX4, and suppressed TfR1, FTH1, LCN2, and p-STING. Pharmacological modulation of STING was associated with changes in these protective effects, while LCN2 inhibition improved iron-homeostasis-related protein expression without substantially affecting p-STING. These findings support a potential role for STING-related signaling and LCN2-associated iron dysregulation in KU-mediated protection against RIR-induced retinal neurodegeneration.

Keywords: Retinal ischemia-reperfusion injury, Kurarinone, STING, LCN2, Ferroptosis

Citation: Shi Y, Zhang N, Zhuo Y, Liao Y, Ma C, et al. 2026. Kurarinone as a potential therapeutic agent targeting the retinal neurovascular unit in ischemic conditions. *Visual Neuroscience* 43: e048 https://doi.org/10.48130/vns-0026-0046

Introduction

Glaucoma comprises a heterogeneous group of progressive optic neuropathies characterized by retinal ganglion cell (RGC) degeneration and corresponding visual field loss[1]. It is projected to affect more than 111.8 million people by 2040[2,3]. A unifying pathological feature across glaucoma subtypes is the progressive loss of RGCs[4]. Although significant progress has been made in understanding the neurodegenerative pathophysiology of glaucoma, clinical treatment remains largely limited to intraocular pressure-lowering strategies[1,5,6]. Clinical studies have revealed elevated levels of numerous chemokines and inflammatory mediators in the aqueous and vitreous humors of patients[7]. Furthermore, multiple lines of experimental evidence suggest that RGC death involves oxidative stress, immune dysregulation, and microglia-mediated neurotoxicity, collectively highlighting the central role of neuroinflammation in the pathogenesis of glaucoma[4,8]. Microglial phagocytosis also contributes to pathological remodeling in the injured retina[9,10]. The dynamic interplay between microglia and retinal cells is increasingly recognized as a key feature of glaucomatous neurodegeneration[11].

Natural products derived from traditional Chinese medicine often exhibit complex structures and potent biological activities, frequently demonstrating promising multitarget therapeutic effects. Notable examples, such as artemisinin and coronavirus disease 2019-related treatments, have garnered global attention[12–14]. Kurarinone (KU), a lavandulylated flavanone isolated from the roots of *Sophora flavescens* Aiton, exhibits potent anti-inflammatory and antioxidative activities[15–17] by modulating transcriptional levels of RORγt and Foxp3 in colonic tissue[18], thereby downregulating the pro-inflammatory cytokine interleukin (IL)-17A while upregulating immunosuppressive factors transforming growth factor-β1 and IL-10. Additionally, KU ameliorated oxidative stress in uveitis by restoring the Th17/Treg balance and enhancing the expression of regulatory mediators in Treg cells[19]. It also mitigated behavioral deficits via the attenuation of dopaminergic neurotoxicity, positioning it as a promising anti-inflammatory and neuroprotective agent[20]. However, whether KU exerts neuroprotective effects in retinal ischemic injury, and the underlying molecular mechanisms, remain unclear.

Aimed at evaluating the therapeutic potential of KU against acute ocular hypertension-induced glaucoma, this study assessed its efficacy in mitigating neuroinflammation and protecting retinal ganglion cells (RGCs). The underlying mechanisms of KU were further deciphered through single-cell RNA sequencing (scRNA-seq) and subsequent *in vitro* validation. Using an LCN2-selective inhibitor, a STING pathway-specific inhibitor, and an activator, we

© The Author(s)

https://doi.org/10.48130/vns-0026-0046

further verified the regulatory relationships involved. Our findings demonstrate that KU serves as a potential neuroprotective agent against glaucoma, with LCN2 identified as a key therapeutic target. These mechanistic efforts align with the broader goal of translating discoveries in visual neuroscience into improved therapies for visual disorders[21].

Materials and methods

Cell culture

The immortalized murine microglial BV-2 cells (RRID:CVCL_0182, Control group) were cultured under standard conditions (37 °C, 5% CO_2) using high-glucose Dulbecco's Modified Eagle Medium (DMEM; Gibco, Thermo Fisher Scientific, USA). Five groups were designed to elucidate the underlying mechanisms: (i) oxygen-glucose deprivation/reperfusion (OGD/R) group; (ii) OGD/R + KU group; (iii) OGD/R + KU + diABZI (T73746, TargetMol, selective agonist of STING); (iv) OGD/R + STING-IN group (T9029, TargetMol, selective inhibitor of STING); (v) OGD/R + KU + LCN2-IN (ZINC00640089, MedChemExpress, selective inhibitor of LCN2) were substituted with glucose-free DMEM (Gibco, Thermo Fisher Scientific, Inc., Waltham, MA, USA), which was then put in a hypoxic incubator (94% nitrogen, 5% carbon dioxide, and 1% O_2) for 4 h at 37 °C to stimulate OGD damage. Following OGD, the medium was substituted with normal glucose DMEM, and cells were returned to a normoxic incubator for a 24-h reperfusion period. Cells in the control (Con) group were kept in high-glucose DMEM supplemented with 10% FBS throughout the experiment.

Cell viability assay

BV-2 cell viability was assessed using the CCK-8 assay (CCK-8; Jiangsu KeyGen Biotech Co., Ltd, Nanjing, China). Cells (5,000/well) were treated with KU (0, 1, 2, 4, and 8 μmol/L) for 24 h, followed by CCK-8 incubation. Absorbance (450 nm) was measured using a microplate reader. Experiments included six replicates per group and were repeated three times.

Reactive oxygen species assay using laser-scanning confocal microscopy

The reactive oxygen species (ROS) assay (D3861; Beyotime Biotechnology, Shanghai, China) was performed according to the manufacturer's instructions. 2′,7′-dichlorodihydrofluorescein diacetate (DCFH-DA) was diluted in DMEM at a 1:1,000 ratio. The original culture medium was aspirated from confocal dishes and replaced with 500 μL DCFH-DA solution in the dark at 37 °C for 30 min. Cells were observed directly using a laser scanning confocal microscope (LSCM) and analyzed using ImageJ software (v1.54p).

FerroOrange assay using laser scanning confocal microscopy

The FerroOrange (F374; Dojindo Laboratories, Kumamoto, Japan) assay was performed according to the manufacturer's protocol. BV-2 cells were harvested and washed three times with DMEM. Then, 1 μmol/L FerroOrange reagent was added in the dark at 37 °C for 30 min. Cells were observed directly using an LSCM and analyzed using ImageJ software (v1.54p).

Animals

All experiments utilized male C57BL/6J mice (6–8 weeks old; 20–25 g) acquired from Beijing Huafukang Bioscience Corporation (Beijing, China). The mice were maintained in a standard barrier environment with a 12/12-h light/dark cycle. The room temperature was 21 ± 1 °C with a humidity of 45% ± 2%. The study protocol received approval from the Animal Care and Ethics Committee of Guangdong Provincial People's Hospital (approval number: No. KY2025-1314-01, approval date: 2026/01/04). All procedures were reported in accordance with the ARRIVE guidelines[22].

Pharmacologic administration and retinal ischemia-reperfusion model

Mice were randomly divided into three groups, and the animals in the different experimental groups were treated and assessed at the same time: (i) sham group (Sham): a 33-gauge needle was used to penetrate the anterior chamber without influencing the IOP; (ii) retinal ischemia-reperfusion (RIR) group: a needle attached to a normal saline bag was used to penetrate the anterior chamber and elevate the IOP to 110 mmHg for 60 min and then reperfusion was conducted for 7 d; (iii) RIR + KU group (RIR + KU): after the mice received KU (20 mg/kg, dissolved in 10% hydroxypropyl-β-cyclodextrin) for 7 d (Fig. 1a). Animal housing and the RIR procedure were conducted as previously described, with minor modifications[23].

Transmission electron microscopy

Retinal tissues were collected 7 d after reperfusion for TEM analysis. The processing protocol included: initial fixation in 2.5% glutaraldehyde (Electron Microscopy Sciences, USA), secondary fixation in 1% osmium tetroxide (Electron Microscopy Sciences), dehydration, and embedding in Epon 812 epoxy resin (Electron Microscopy Sciences). Finally, 70 nm ultrathin sections were stained and processed for imaging on a JEM-1230 TEM.

Hematoxylin and eosin staining

Fresh eyeballs were extracted and fixed in 4% paraformaldehyde (PFA; Sigma-Aldrich, St. Louis, MO, USA) for more than 24 h. The samples were dehydrated using ethyl alcohol and embedded in paraffin (Sigma-Aldrich, St. Louis, MO, USA). The cell nucleus was stained with hematoxylin, and the cytoplasm was stained with eosin (H&E; Beyotime Biotechnology, Shanghai, China). Data were analyzed using ImageJ software (v1.54p).

Immunofluorescence staining (including dihydroxyethidium and terminal deoxynucleotidyl transferase-mediated dUTP nick end labeling)

Mice were anesthetized with pentobarbitalum natricum (Sigma-Aldrich, St. Louis, MO, USA) and perfused with saline/4% PFA. Eyeballs were fixed, dehydrated in 30% sucrose (Sakura Finetek, Torrance, CA, USA), OCT-embedded, and sectioned. Sections were blocked and incubated with primary antibodies (Supplementary Table S1). After PBS washes, secondary antibodies were applied, followed by DAPI staining (Bioss). For TUNEL, sections were treated with proteinase K (Servicebio, Wuhan, China), equilibrated, and labeled with TdT mix (Servicebio). Images were acquired on a Leica DMi8 immunofluorescence microscope.

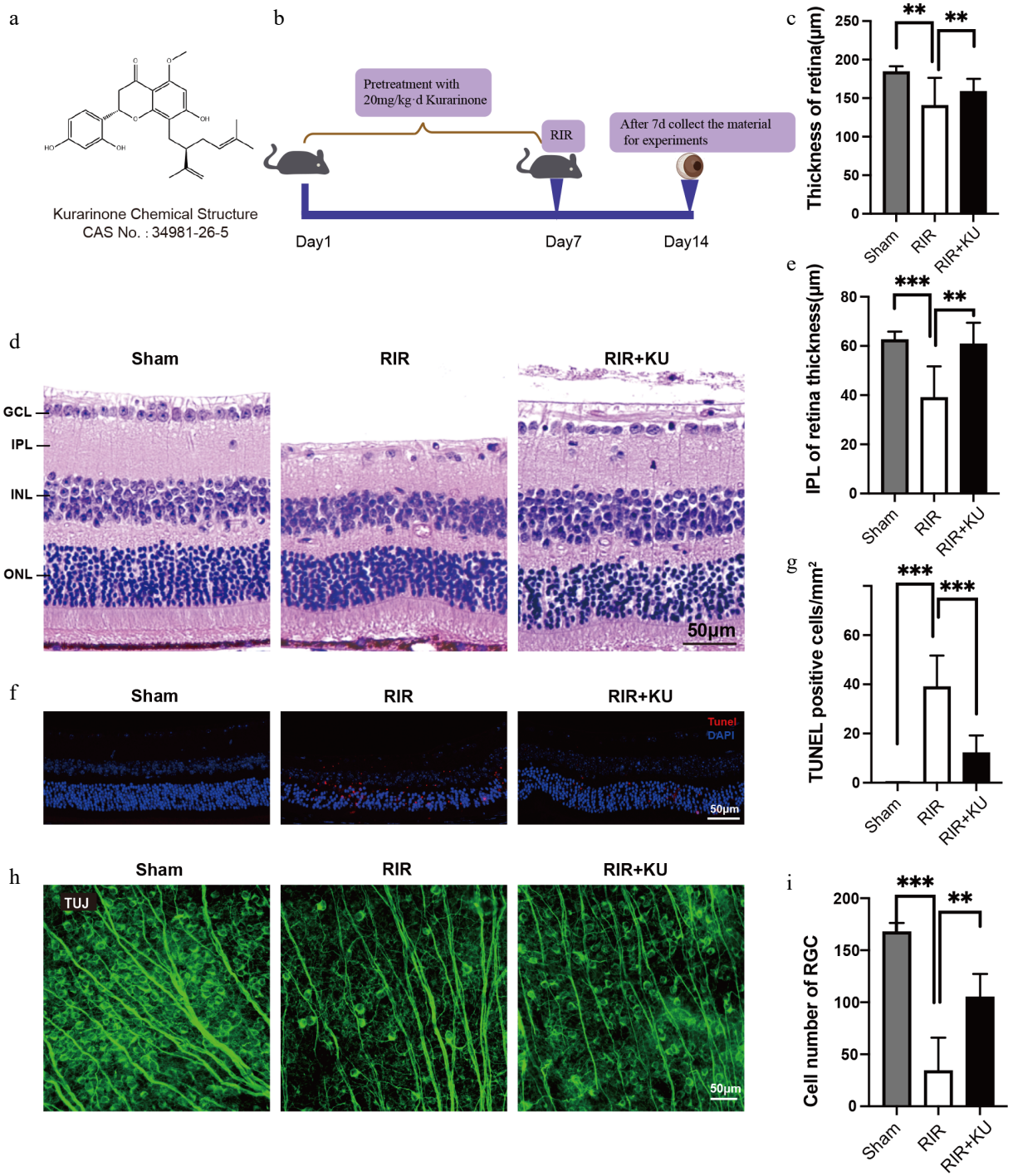

Fig. 1 KU treatment attenuated RIR-induced RGC death in mice. (a) Chemical structure of KU. (b) Schematic of the experimental design. (c) Comparison of retinal H&E section images showing the characteristics of Sham, RIR, and RIR + KU. (d) H&E-stained retinal morphology across experimental groups. Scale bar = 50 μm. (e) Measurements of IPL and overall retinal thickness (n = 4–6 mice per group; two sections per mouse). (f) Co-staining of TUNEL (apoptotic cells, red) and DAPI (nuclei, blue) in retinal slices. Apoptotic cells were absent in the Sham group, increased after RIR, and decreased with KU. Scale bar = 50 μm. (g) Quantification of the number of TUNEL-positive cells in the entire retina (n = 4 mice per group and two retinal sections for each mouse). (h) Representative images of TUJ staining (RGC marker) in retinal flat mounts. Scale bar = 50 μm. (i) Quantification of the number of RGCs in the selected region (n = 6 mice per group). ** $p < 0.01$; *** $p < 0.001$.

Quantitative real-time polymerase chain reaction (qRT-PCR)

RNA was extracted using the RN002 RNA-Quick Purification Kit (ESscience, Shanghai, China), reverse transcribed using PrimeScript RT Master Mix (Takara, Kyoto, Japan), and amplified using qPCR (LightCycler® 480, Roche Diagnostics, Basel, Switzerland). Gene expression was normalized to GAPDH, with primers listed in Supplementary Table S2.

https://doi.org/10.48130/vns-0026-0046

Western blot

Mouse retinal proteins were extracted using a KeyGEN (Jiangsu, China) whole-cell lysis assay. The proteins were subjected to SDS-PAGE (YaMei, Shanghai, China), transferred to a PVDF membrane (Millipore, USA), and blocked with 5% milk. Incubations were carried out with primary antibodies (Supplementary Table S1) and subsequently with HRP-conjugated secondary antibodies. Detection was achieved using a Bio-Rad (USA) chemiluminescence system.

Flow cytometric analysis of CD11b+ cells

After retinas were collected 7 d post-reperfusion, cells were obtained by homogenization. The cells were stained with live/dead cell dyes and surface antibodies, followed by permeabilization, fixation, and staining with FITC-conjugated anti-CD11b (Supplementary Table S1). Samples were analyzed using an Attune™ NxT Flow Cytometer (Invitrogen, USA), and the data were analyzed using FlowJo (v10.0).

Single-cell genomics

scRNA-seq datasets

To investigate the molecular mechanisms underlying retinal ischemia and glaucoma, we extracted six published mouse single-cell datasets from our previously published studies[24] and integrated them with the single-cell data from the KU group in this study (Supplementary Table S1). The combined dataset comprised 54,270 cells and 20,960 genes. A Seurat object was created using the CreateSeuratObject function, followed by further downstream data analysis.

Single-cell data integration and annotation

Single-cell data were annotated using Seurat. Data were normalized (SCTransform), integrated (Harmony, PCA = 120), and clustered (SNN: k = 60, PCs = 80; resolution = 1.2) into 44 clusters, visualized using UMAP. Differentially expressed genes were identified (FindAllMarkers; min.pct = 0.1, logfc.threshold = 1.5; Bonferroni $p < 0.05$), and clusters were annotated into 16 cell types based on DEGs.

Gene ontology (GO) and KEGG enrichment analysis

Functional enrichment analysis for DEGs was carried out with the clusterProfiler R package (v4.6.2). Specifically, GO biological processes and KEGG pathways were interrogated via over-representation tests (enrichGO/enrichKEGG), considering terms with an adjusted p-value < 0.05 as statistically significant.

Gene set enrichment analysis

DEGs ($|\log_2FC| > 1.5$, adj. $p < 0.05$) ranked according to $\log_2FC$ were identified using differential expression analysis (Seurat FindMarkers). GSEA (fgsea) of KEGG/GO:BP pathways (MSigDB) was performed using this ranking. The analysis was repeated specifically in the microglial subpopulation.

Cell trajectory analysis

Myeloid cell trajectories were analyzed using differentially expressed genes identified with Seurat FindAllMarkers[25]. We filtered these differentially expressed genes based on abs (avg_log2FC > 1) and p_val_adj < 0.05. Cell state transitions were constructed using Monocle3 (new_cell_data_set, learn_graph).

Cell–cell communication analysis

Cell communication was analyzed using CellChat, which computed intercellular networks and predicted key signaling pathways by analyzing only receptors/ligands expressed in ≥ 10% of cells.

Cell purity analysis

Cluster purity was validated using ROGUE, a computational metric for unsupervised scRNA-seq data that quantifies the purity of cell populations.

Protein interaction analysis

Potential protein–protein interactions were retrieved from the STRING database (https://string-db.org) for network analysis.

Gene set scoring analysis

To delineate the role of the ferroptosis pathway within the context of glaucomatous neuroinflammation, we compiled three ferroptosis-related gene sets (detailed in Supplementary Tables S3–S5). Single-cell enrichment scores were computed with Seurat's AddModuleScore, normalizing gene set expression against binned control features.

Transcription factor analysis

Transcriptional networks governing diverse retinal cell populations were delineated through pySCENIC-based transcription factor (TF) analysis, which utilized the raw single-cell expression matrix as input, with results visualized in R.

Molecular docking

Molecular docking simulations were conducted between the receptor STING (PDB: 6UL0) and ligand NFYA (PDB: 6QMP) using a locally implemented HDOCK1.1 platform. The simulation generated 100,000 sampling poses, from which the 10 most favorable conformations ranked according to docking score were selected for further analysis.

Statistical analysis

Statistical significance was calculated using one-way analysis of variance, followed by Tukey's multiple comparison test among multiple groups or the unpaired Student's t-test between two groups. Figure creation and calculations were performed using GraphPad. Statistical analysis of scRNA-seq was performed using the R3.6.0 framework. The Benjamini–Hochberg method was employed for p-value adjustment to account for multiple comparisons, with statistical significance denoted by asterisks: **** $p < 0.0001$, *** $p < 0.001$, ** $p < 0.01$, and * $p < 0.05$.

Results

KU treatment attenuated RIR-induced RGC death in mice

KU, a colorless crystalline compound (Fig. 1a), was obtained commercially. Its structural identity was confirmed by LC-MS, and its purity was verified using HPLC. The study design is illustrated in Fig. 1b. To evaluate the effect of KU pretreatment on RGC loss 7 d after RIR, H&E staining was performed. The results showed that RIR exposure induced an average reduction of 43.72 ± 12.14 μm in the overall retinal thickness and a decrease of 23.51 ± 4.363 μm in the IPL thickness. The retinal cells in the RIR injury group exhibited disorganized arrangement and vacuolation. However, pretreatment with KU (20 mg/kg) significantly improved the architecture of retinal layers, accompanied by increases of 33.25 ± 15.3 μm and 21.79 ± 5.499 μm (Fig. 1c–e). Because apoptosis is a major pathological process in RIR injury, we assessed cell death using the TUNEL assay. Compared to the RIR injury group, the number of TUNEL-positive cells was significantly reduced in retinas treated with KU (Fig. 1f).

RGCs were specifically labeled using IF staining. Quantitative evaluation of RGC density in retinal flat mounts (Fig. 1g) consistently demonstrated that RIR injury decreased the RGC survival rate, an effect that was markedly prevented by KU pretreatment. IF staining of whole-mount retinas for β-tubulin III (Tuj-1) revealed a decrease in RGC density 7 d after reperfusion. KU pretreatment effectively rescued RGC loss (Fig. 1h, i). These data suggest that pretreatment with KU (20 mg/kg) has neuroprotective effects, ameliorating RIR-induced RGC damage within the 7-d acute phase following injury.

KU reduces oxidative stress and glial cell activation after retinal RIR injury

Classically activated glial cells mediate the production of various pro-inflammatory cytokines, including TNF-α, IL-1β, and IL-6, along with ROS, as part of the defense mechanism against stress and damaged tissue clearance. KU pretreatment significantly suppressed the upregulation of these inflammatory factors and their associated ROS production, indicating that KU exhibited both anti-inflammatory and antioxidative stress properties (Fig. 2a, b). Furthermore,

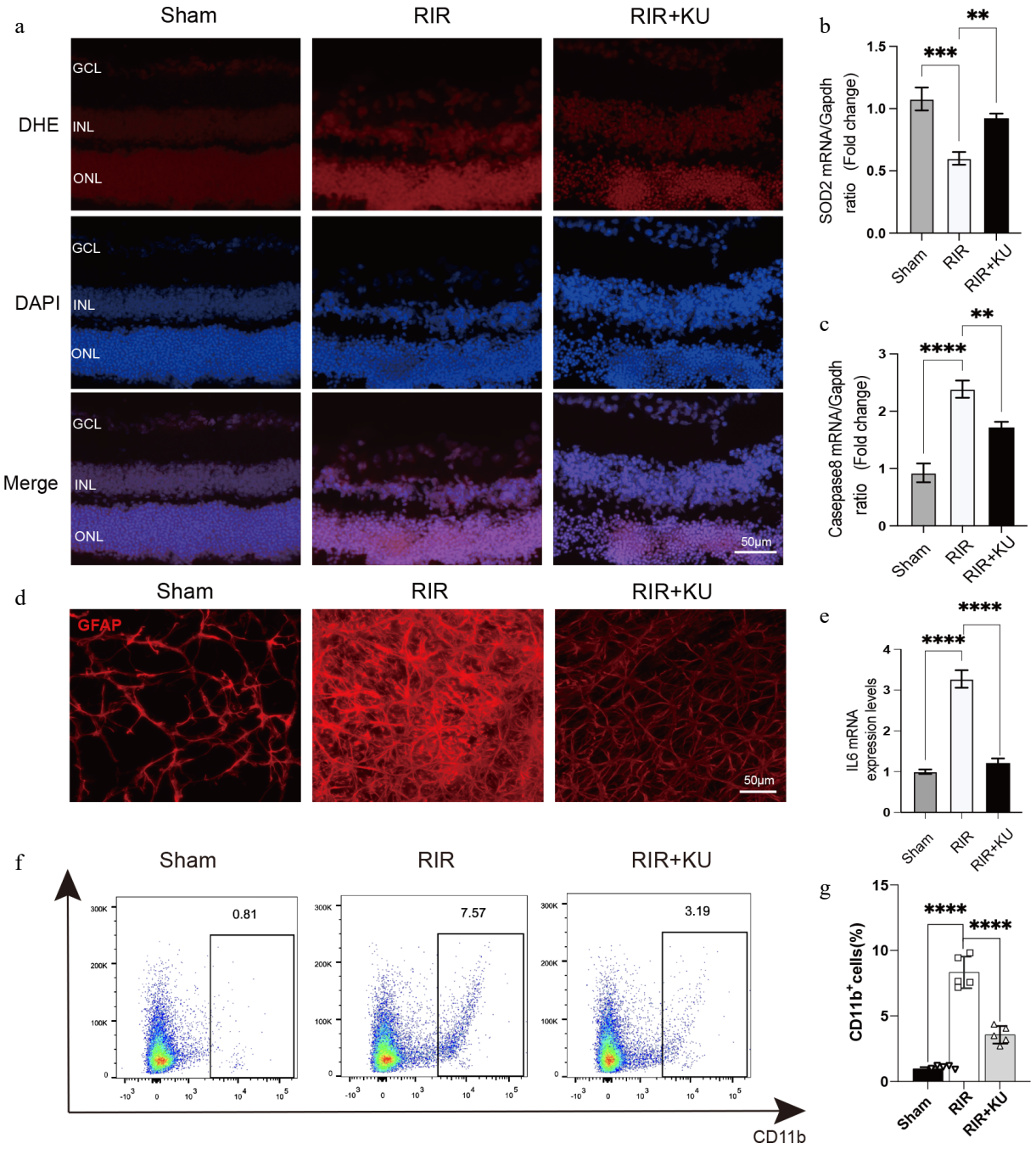

Fig. 2 KU reduces oxidative stress and glial cell activation after retinal RIR injury. (a) DHE staining shows ROS production in retinal sections. The RIR group exhibited increased ROS levels, an effect reduced by KU. Scale bar = 50 μm. (b), (c) Relative mRNA expression of the inflammatory indicators (SOD2 and Caspase8) in all groups. (d) Retinal whole-mounts revealed alterations in the reactivity and density of astrocytes (GFAP, red staining). Scale bar = 50 μm. (e) Relative mRNA expression of the inflammatory indicator (*Il-6*) in all groups. (f) Flow cytometry was used to detect changes in the number of microglia. (g) Quantitative analysis of flow cytometry results. ** $p < 0.01$, *** $p < 0.001$,**** $p < 0.0001$.

https://doi.org/10.48130/vns-0026-0046

retinal whole-mount analysis demonstrated a notable reduction in GFAP immunoreactivity following KU pretreatment, reflecting significant inhibition of astrocyte activation induced by RIR (Fig. 2d). To further assess the inflammatory response, we examined the relative mRNA expression of *Caspase-8* and *IL-6* across all groups (Fig. 2c, e). Flow cytometry further revealed that the increase in $CD11b^+$ cells observed after RIR injury was markedly attenuated by KU treatment (Fig. 2f, g). These findings collectively suggest that KU alleviates RIR injury by reducing ROS levels and suppressing the activation of both microglia and astrocytes.

KU treatment reprogrammed the immune cell landscape in RIR

Single-cell RNA sequencing (scRNA-seq) was performed to examine cell-type composition and transcriptional profiles in the retina after KU treatment (Fig. 3a; Supplementary Fig. S1). To obtain a sufficient number of cells for sequencing, retinas from four independent KU + RIR-treated animals were pooled into a single sample. After stringent quality control, 54,270 cells were retained for downstream analysis, including 9,195 cells from the Sham group, 24,159 cells from the RIR group, and 20,916 cells from the KU-treated group. Forty-four cell clusters were defined and annotated based on classical marker genes, yielding 16 cell types (Fig. 3b; Supplementary Fig. S2a, S2b). We examined changes in cell proportions after RIR and KU treatment (Supplementary Fig. S2c); immune-cell populations, including lymphocytes and myeloid cells, were increased after RIR and were lower in the KU-treated group. Annotation quality is shown in Supplementary Fig. S2d. In the KU-treated group, enrichment analyses identified terms associated with neuronal and visual system processes (Fig. 3c, d, g). Inflammatory scoring was consistent with the earlier experimental observations (Fig. 3e, f). GSEA showed negative enrichment of gene sets associated with microglial activation (normalized enrichment score [NES] = −2.83, adjusted $p < 0.001$) and cellular stress response (NES = −1.56, adjusted $p < 0.001$) in the KU-treated group (Fig. 3h, i). These analyses identify candidate transcriptional changes associated with KU treatment; targeted molecular validation is required to establish pathway activity or causal involvement.

KU pretreatment inhibited ferroptosis-associated changes in microglial cells after RIR

In the central nervous system, microglia have a high iron-storage capacity and may accumulate iron under pathological conditions. Our previous study[18] reported that iron overload impairs microglial function and that iron-laden microglia contribute to RIR injury. To explore whether KU was associated with iron-related transcriptional changes after RIR, we analyzed differentially expressed genes from the RIR and KU-treatment comparisons (Fig. 3h, d). The analysis identified gene sets annotated to oxidative stress, cell activation, and ferroptosis. In the KU-treated comparison, some ferroptosis-related genes showed partial reversal relative to the RIR group (Fig. 4a). These transcript-level observations identify candidates for further validation and do not, by themselves, establish ferroptosis activity.

Uniform manifold approximation and projection visualization and gene-signature scoring suggested that ferroptosis-related transcriptional signatures were most prominent in microglia, neutrophils, and monocytes (Fig. 4b–d). This observation was supported by ferroptosis-related gene-signature scoring in isolated microglial cells (Fig. 4e–g, i; gene sets were obtained from the FerrDb database www.zhounan.org/ferrdb/current). Because mitochondrial damage is a reported feature of ferroptosis, we used electron microscopy to assess mitochondrial morphology in the RIR model; the images were consistent with improved mitochondrial morphology after KU pretreatment (Fig. 4h). We also measured key iron transport regulators. As shown in Fig. 4j, RIR increased TFR and FTH1 expression and decreased NCOA4 levels. GSEA using publicly available gene sets showed negative enrichment of signatures related to the ROS metabolic process (NES = −3.13, adjusted $p < 0.001$; Fig. 4k), metal-ion transport (NES = −1.60, adjusted $p = 0.02$; Fig. 4l), and innate immune response (NES = −4.13, adjusted $p < 0.001$; Fig. 4m) in KU-treated retinas. These genomic analyses are hypothesis-generating and require targeted molecular validation.

KU protects microglial cells from ferroptosis-associated changes by inhibiting the STING pathway

The STING signaling pathway is a critical signaling cascade that becomes significantly upregulated under inflammatory conditions. This pathway enables cells to sense and respond to the presence of cytosolic double-stranded DNA (dsDNA). By inducing the expression and secretion of type I interferons and interferon-stimulated genes, it establishes a potent innate immune response.

Therefore, we investigated whether the inhibitory effect of KU on microglial ferroptosis under ischemic-reperfusion conditions was associated with the STING pathway. First, we assessed the potential cytotoxicity of KU in microglial cells by incubating BV2 cells with various concentrations of KU for 24 h. CCK-8 results indicated that low concentrations of KU (2 μmol/L) did not affect cell viability; therefore, this concentration was selected for subsequent experiments (Fig. 5a, b).

In ferroptosis, iron promotes the generation of lipid reactive oxygen species (ROS) via the Fenton reaction. Therefore, we evaluated redox-related indicators by measuring ROS levels using a ferroptosis assay kit to assess ferroptosis levels. OGD/R significantly increased ROS production and ferroptosis, whereas KU treatment effectively reduced ROS production and the number of ferroptotic cells. Notably, these protective effects were reversed upon administration of the STING agonist (Fig. 5c–f).

To examine the potential relationship between STING-pathway modulation and iron-regulatory proteins, we analyzed proteins involved in iron uptake (transferrin receptor 1 [TFR1]), iron export (ferroportin [FPN]), iron storage (ferritin heavy chain 1 [FTH1]), and suppression of lipid-peroxidation toxicity (glutathione peroxidase 4 [GPX4]). KU treatment increased FPN and GPX4 and reduced TFR1 and FTH1 levels (Fig. 5g). Treatment with the STING-pathway inhibitor produced a similar pattern of changes in these iron-regulatory proteins (Fig. 5g), consistent with a possible contribution of STING-related signaling. Total STING protein expression was not measured in the STING-inhibitor groups.

These findings demonstrate that OGD/R disrupts iron homeostasis and that KU exerts a comprehensive effect on the critical nodes of the iron metabolic network. It restores the balance in iron metabolism by enhancing FPN-mediated iron export and inhibiting TFR1- and FTH1-mediated iron uptake and storage.

LCN2 is the pivotal regulator through which KU orchestrates its anti-inflammatory and anti-ferroptotic activities

To systematically elucidate the mechanism by which KU protects the retina from RIR injury, we performed single-cell transcriptomic analysis of microglia from the Sham, RIR, and RIR + KU groups. This

https://doi.org/10.48130/vns-0026-0046

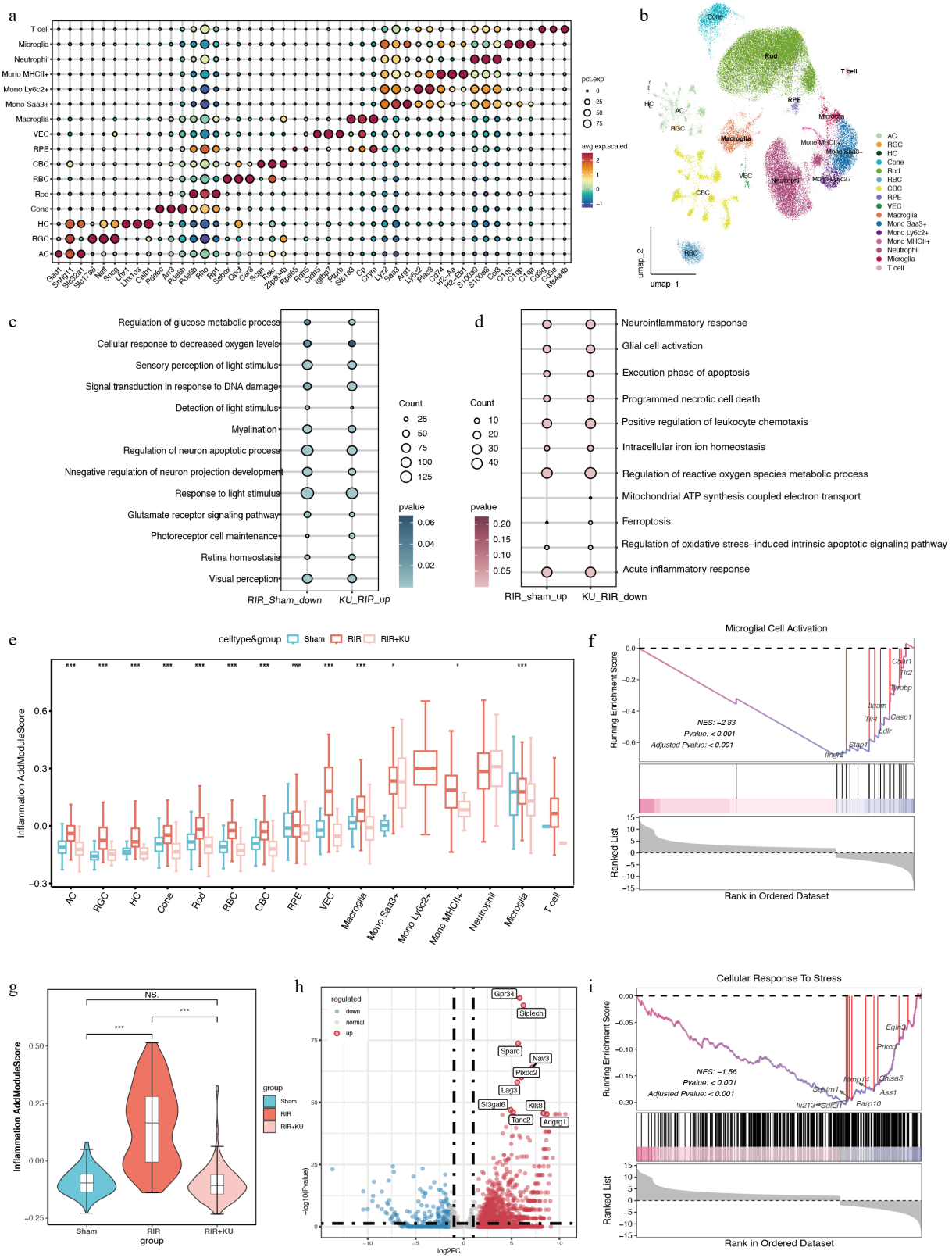

Fig. 3 KU treatment reprogrammed the immune cell landscape in RIR. (a) Dot plot showing the scaled expression of the top three marker genes for each cell type. (b) UMAP showing the clustering of different cell types in the pooled retina. Dot plot showing the functional GO analysis of (c) downregulated and (d) upregulated DEGs among the three groups. (e) Box plot displays the inflammatory scores across different cell types (median center line; 25th/75th percentiles as box limits). (f) Representative gene set enrichment analysis plots showing signatures of the GO biological process response to microglial activation. (g) Violin plot presents the inflammatory score distribution among the three groups (median and interquartile range shown by the central line and plot edges, respectively). (h) Volcano plot showing the DEGs of whole retinas (RIR vs RIR + KU). (i) Representative gene set enrichment analysis plots showing signatures of the cellular response to stress in RIR + KU retinas.

https://doi.org/10.48130/vns-0026-0046

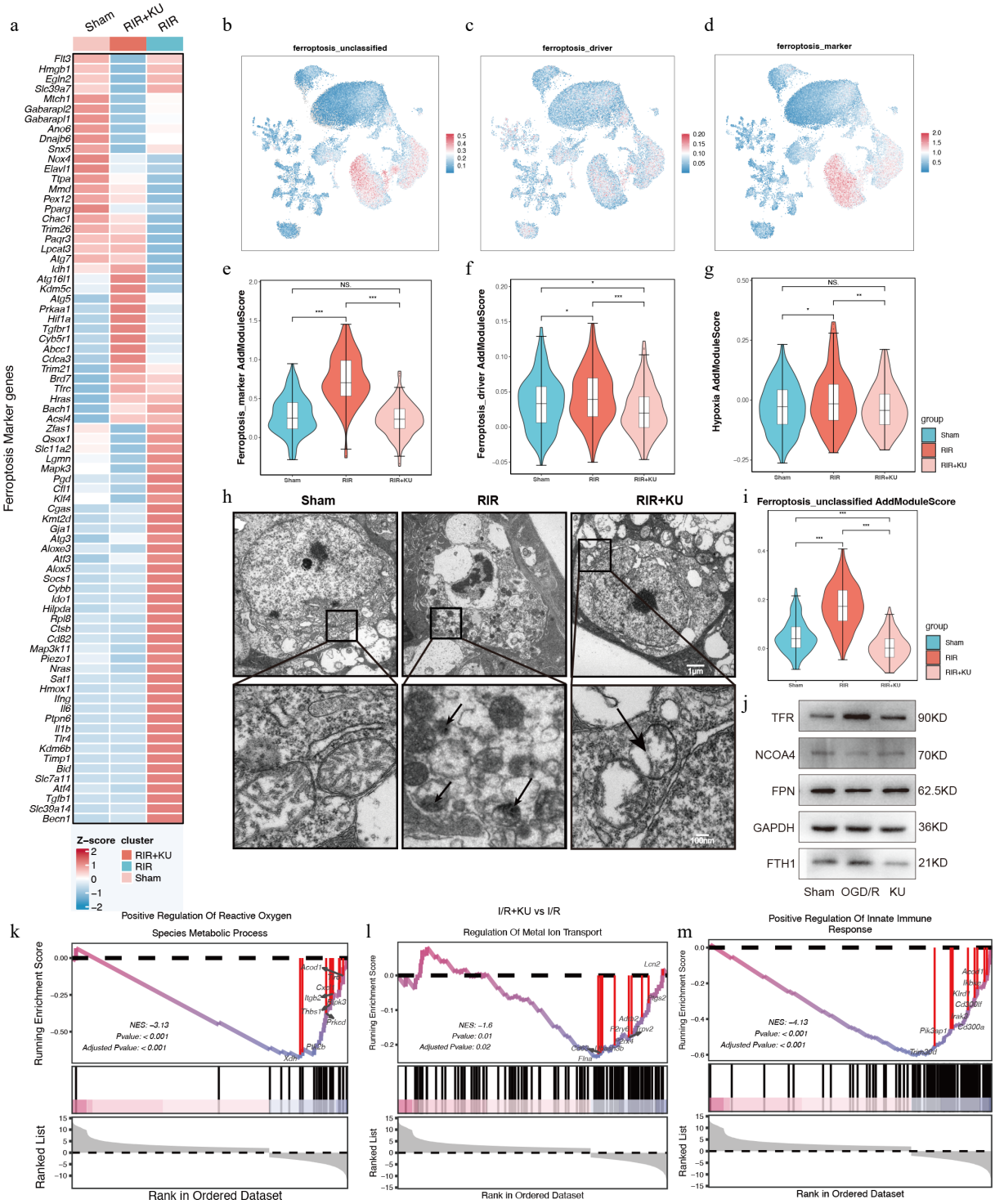

Fig. 4 Ferroptosis was increased in the microglia and decreased by KU treatment. (a) Heatmap showing the expression of ferroptosis-marker genes across the three groups. UMAP plot showing the distribution of ferroptosis-related gene set enrichment scores across retinal single-cell clusters: (b) unclassified ferroptosis genes, (c) ferroptosis driver genes, and (d) ferroptosis-associated markers. The color gradient represents enrichment scores, with red indicating elevated ferroptosis-related gene expression and blue indicating diminished activity. Each point represents an individual cell, with point coordinates determined by UMAP dimensionality reduction. Violin plots showing the ferroptosis-related gene scores across the three groups: (e) ferroptosis-associated marker gene set, (f) ferroptosis driver gene set, and (g) hypoxia gene set. In each violin plot, the middle line indicates the median and the bottom and upper lines indicate the 25th and 75th percentiles, respectively. * $p < 0.05$, ** $p < 0.01$, *** $p < 0.001$. (h) Representative transmission electron microscopy (TEM) showing the mitochondrial structure and cristae morphology (black arrows). Scale bar = 1 μm (upper image) or 100 nm (lower image). (i) Violin plot showing the ferroptosis suppressor gene score across the three groups. In each violin plot, the middle line indicates the median and the bottom and upper lines indicate the 25th and 75th percentiles, respectively. (j) Representative western blot analysis of iron homeostasis-related markers (TFR, NCOA4, FPN, and FTH1) in microglia. GSEA results of positive regulation of the (k) ROS metabolic process, (l) regulation of metal ion transport, and (m) positive regulation of the innate immune response in RIR + KU retinas.

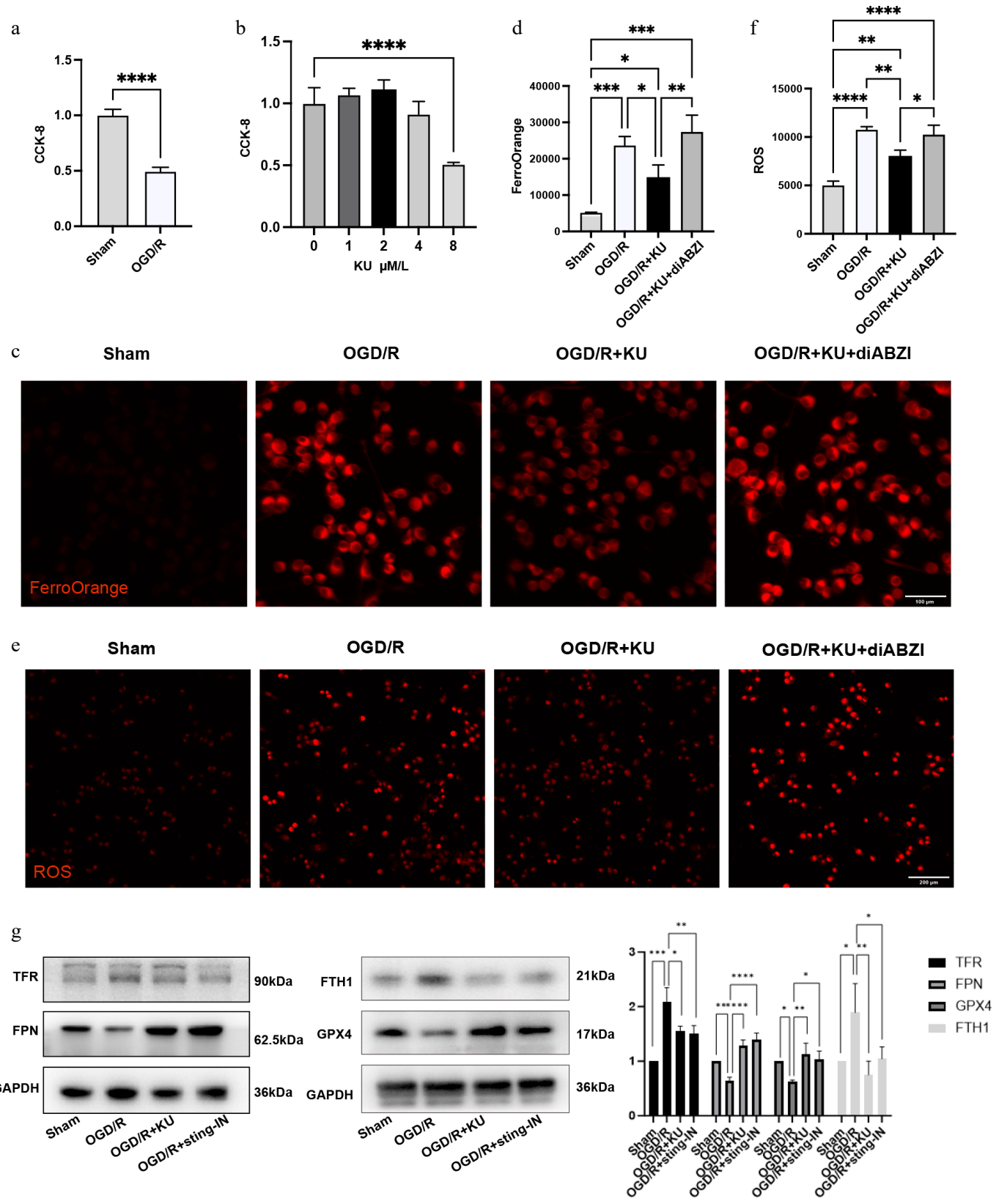

Fig. 5 KU suppresses ferroptosis by inhibiting the STING pathway and reducing intracellular free ferrous iron. (a) CCK-8 assay for microglial viability under OGD/R. (b) CCK-8 assay for KU cytotoxicity. (c) Confocal microscopy images depicting FerroOrange staining (red), indicating ferrous iron localization in viable microglia under OGD/R conditions, with or without KU and diABZI treatments. Scale bar = 100 μm. (d) Quantitative analysis of FerroOrange fluorescence intensity. (e) Representative images showing mitochondrial ROS detection by DHE staining (red). Scale bar = 200 μm. (f) Quantitative results of the fluorescence intensity of ROS. (g) Western blot analysis of TFR, FPN, FTH1, and GPX4 protein expression levels. Data are expressed as mean ± SD. * $p < 0.05$, ** $p < 0.01$, *** $p < 0.001$, **** $p < 0.0001$.

https://doi.org/10.48130/vns-0026-0046

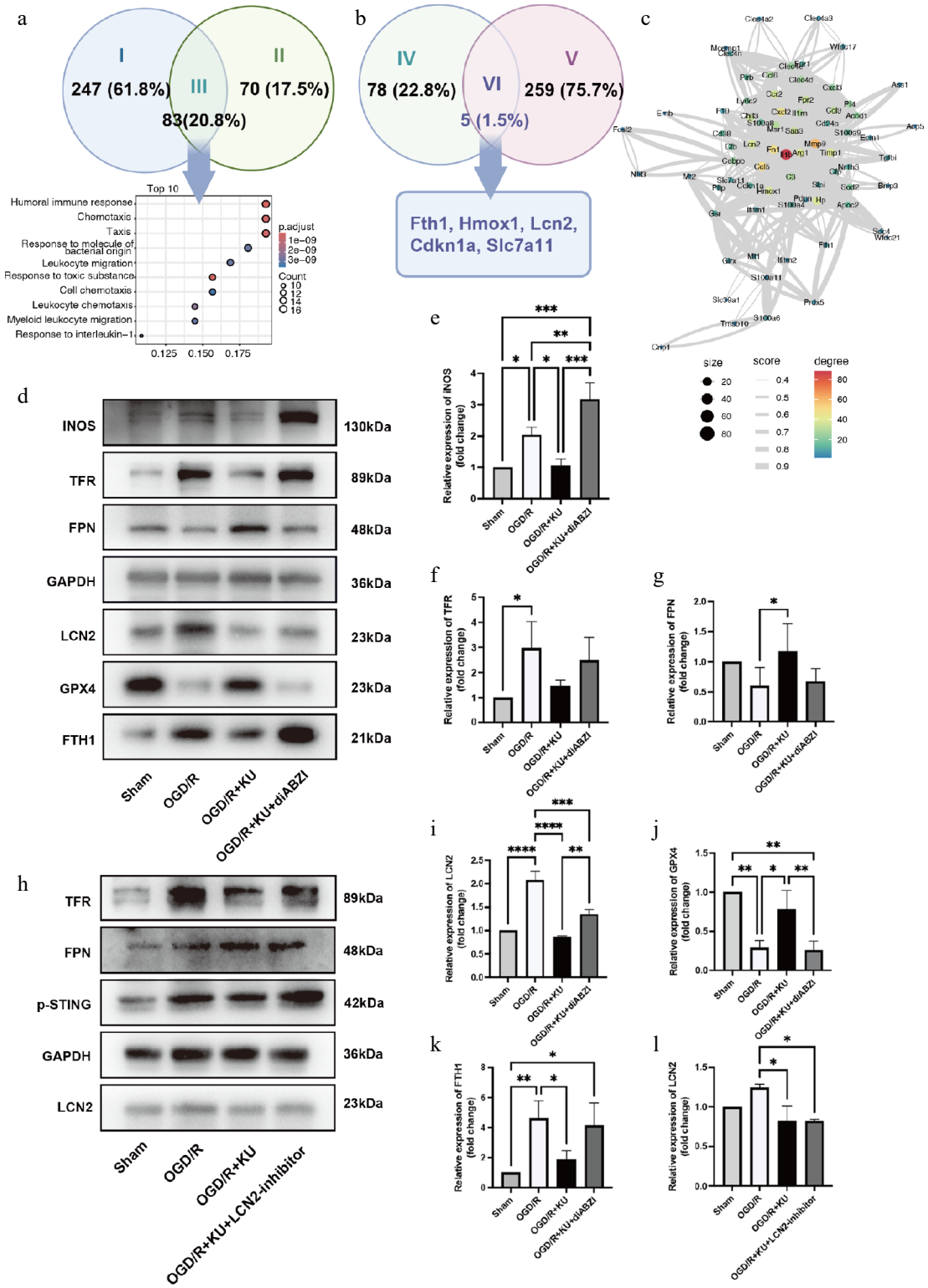

Fig. 6 LCN2 plays a critical role in KU-mediated suppression of ferroptosis. (a) Venn diagram of DEGs in microglia across the three groups, and the top 10 KEGG pathways enriched in the 83 overlapping genes. (I) Genes upregulated in microglia following RIR versus Sham (n = 330). (II) Genes downregulated by KU treatment compared to RIR (n = 153). (III) Overlap between (I) and (II) datasets (n = 83). (b) Venn diagram depicting the overlap between KU-regulated key genes in microglial inflammation and the ferroptosis suppressor gene set. (IV) Overlap between (I) and (II) datasets (n = 83). (V) Ferroptosis suppressor gene set (n = 264). (VI) Overlap between datasets (IV) and (V) (n = 5). (c) A protein–protein interaction network was generated from the 83 DEGs (identified in the Venn analysis, Fig. 6a[III]) using STRING. (d) iNOS, TFR, FPN, LCN2, GPX4, and FTH1 protein expression levels in microglia treated with OGD/R, OGD/R + KU or OGD/R + KU + diABZI. Representative protein expression by western blot analysis. (e) Relative protein expression of iNOS. (f) Relative protein expression of TFR. (g) Relative protein expression of FPN. (h) TFR, FPN, p-STING, and LCN2 protein expression levels in microglia treated with OGD/R, OGD/R + KU, or OGD/R + KU + LCN2 inhibitor. (i) Relative protein expression of LCN2. (j) Relative protein expression of GPX4. (k) Relative protein expression of FTH1. (l) Relative protein expression of LCN2. Data are expressed as mean ± SD. * p < 0.05, ** p < 0.01, *** p < 0.001, **** p < 0.0001.

led to the identification of 83 core genes (avg_log$_2$FC > 1.5, p_value < 0.05) that were upregulated following RIR and subsequently downregulated by KU treatment (Fig. 6a). To pinpoint genes involved in ferroptosis regulation among these 83 candidates, we intersected them with a ferroptosis suppressor gene set, yielding five overlapping genes (Fig. 6b). Subsequently, protein–protein interaction (PPI) network analysis of the 83 core proteins identified the top 10 hub proteins as IL1β, MMP9, CCL5, FN1, CXCL2, ARG1, TIMP1, LCN2, HMOX1, and HP. Notably, LCN2 was the only one among the five key ferroptosis-related genes that also ranked among the top ten hub proteins in the PPI network (Supplementary Table S6). Further analysis of LCN2 expression across different cell types confirmed its relatively high abundance in microglia (Supplementary Fig. S2), supporting its suitability for subsequent experimental validation. Based on these findings, we identified LCN2 as a central hub gene linking inflammatory and ferroptotic processes (Fig. 6c).

Western blot analysis showed that KU was associated with changes in OGD/R-induced microglial protein expression, including reduced LCN2 expression and changes in ferroptosis-related markers. Co-treatment with the STING agonist diABZI attenuated these KU-associated effects (Fig. 6d–j). When an LCN2 inhibitor was applied together with KU, LCN2 suppression was maintained, p-STING expression was not substantially changed, and the changes in TFR and FPN were comparable to those observed with KU treatment alone (Fig. 6k, l). This pattern is consistent with LCN2 functioning downstream of STING-related signaling; however, the pharmacological data do not establish a direct regulatory relationship.

NFYA is predicted as a candidate regulator of LCN2, downstream of STING-associated signaling

To identify upstream regulators of LCN2, we analyzed transcription factor (TF) profiles across different retinal cell types (Fig. 7a). Venn diagram analysis of TFs from major databases (hTFtarget and KnockTF) predicted 16 potential upstream transcription factors for LCN2 (Fig. 7c). Among these 16 candidates, NFYA was identified as a representative transcription factor in microglia. Subsequently, we performed molecular docking to simulate the binding energy between STING and NFYA. The results demonstrated a strong binding affinity between STING and NFYA, with an HDOCK score of −238.94, significantly below the −200 threshold indicative of stable binding (Fig. 7b). This interaction was stabilized by eight hydrogen bonds formed between residues ASP-210, ASN-211, VAL-239, THR-263, GLN-266, and THR-267 of STING and LYS-271, GLN-272, ARG-275, ARG-280, and ARG-283 of NFYA (Fig. 7d), suggesting that STING may influence LCN2 transcription through its binding to NFYA.

In summary, the findings are consistent with a working model in which KU may ameliorate RIR injury through STING-related signaling and LCN2-associated regulation of iron homeostasis in microglia (Fig. 7e). Further molecular and genetic validation is required to define the proposed pathway and its causal relationships.

Discussion

In this study, we investigated the effects of KU against acute ocular hypertension-induced RIR injury using *in vivo* and *in vitro* approaches. KU pretreatment was associated with preservation of retinal architecture, reduced RGC loss, and attenuation of oxidative stress and glial activation. In OGD/R-challenged microglia, KU was associated with lower reactive oxygen species and Fe^{2+} accumulation and with changes in iron-regulatory proteins. The single-cell and enrichment analyses identified candidate inflammatory and ferroptosis-related transcriptional programs, but they do not alone establish pathway activity or causality. Pharmacological modulation of STING and LCN2 yielded patterns consistent with the involvement of STING-related signaling and LCN2-associated iron dysregulation. These findings should be interpreted cautiously because total STING protein levels were not measured in the STING-inhibitor experiments and genetic confirmation was not performed.

Natural products derived from traditional Chinese medicine have increasingly been investigated as sources of bioactive compounds for neuroprotection. Several phytochemicals, including baicalein and puerarin, have shown protective effects in experimental models of glaucomatous retinal injury. Qi, blood, and body fluids also get stuck. They treat by spotting the pattern first, then pick the fix. Previous studies showed that mixtures like Qingguang'An II soup, Baicalein, and Puerarin help guard against the disease[26–29]. Although the components of Chinese herbal medicines and their interactions in glaucoma are highly complex, exploring the underlying molecular mechanisms through single-cell sequencing is feasible. This study focuses on the inflammatory and immune landscape during acute ocular hypertension-induced retinal ischemia-reperfusion (RIR) injury and the specific therapeutic mechanisms of KU. Our previous findings[26] established the significant role of ferroptosis in RIR pathogenesis; these new data add that KU brakes the snowballing neuroinflammatory noise by simply stopping microglial ferroptosis. The cGAS/STING pathway is a central innate immune signaling pathway that senses cytosolic DNA and induces type I interferon and other inflammatory gene programs[30–32]. Persistent activation of this pathway has been implicated in inflammatory disorders. Previous studies in THP-1 cells and bone-marrow-derived macrophages reported that kurarinone can promote STING destabilization and degradation. In the present study, the pharmacological findings are consistent with a role for STING-related signaling in retinal microglia during RIR. However, because total STING protein expression was not assessed in the STING-inhibitor experiments, we cannot determine whether KU alters STING abundance in this model. Studies measuring total STING and downstream pathway activity, together with genetic perturbation, will be needed to define the mechanism.

LCN2 has emerged as an important regulator of inflammation and iron homeostasis. Researchers continue to point to its iron-binding and iron-transport functions. LCN2 is a secreted glycoprotein released by cells; once outside, it participates in inflammation, growth, specialization, and even cell death[33–35]. Notably, the effects of LCN2 on ferroptosis appear highly context-dependent, and these observations have led to increasing interest in an LCN2–ferroptosis regulatory axis, for example in pancreatic cancer[36], liver tumors[37], and scarred liver[38]. In these settings, LCN2 captures free iron and sequesters it, leaving less iron for Fenton chemistry and lipid peroxidation, thereby keeping cells alive; this protective shield helps the disease progress[39,40]. Conversely, in skeletal muscle injury[41], intracerebral hemorrhage[42], chronic kidney disease-related vascular calcification[43], and certain degenerative conditions[44], LCN2 acts as a ferroptosis promoter by exacerbating iron accumulation or impairing antioxidant systems, leading to cell death and tissue damage[45]. This functional duality stems from distinct cellular demands and regulatory mechanisms governing iron metabolism and oxidative stress in different pathological settings[46–48]. In our acute ocular hypertension model, LCN2 was significantly upregulated (Supplementary Fig. S2b, S2e), consistent with its iron-sequestering, ferroptosis-suppressing role. Protein–protein interaction screening further identified LCN2 as a key mediator in KU-induced ferroptosis

https://doi.org/10.48130/vns-0026-0046

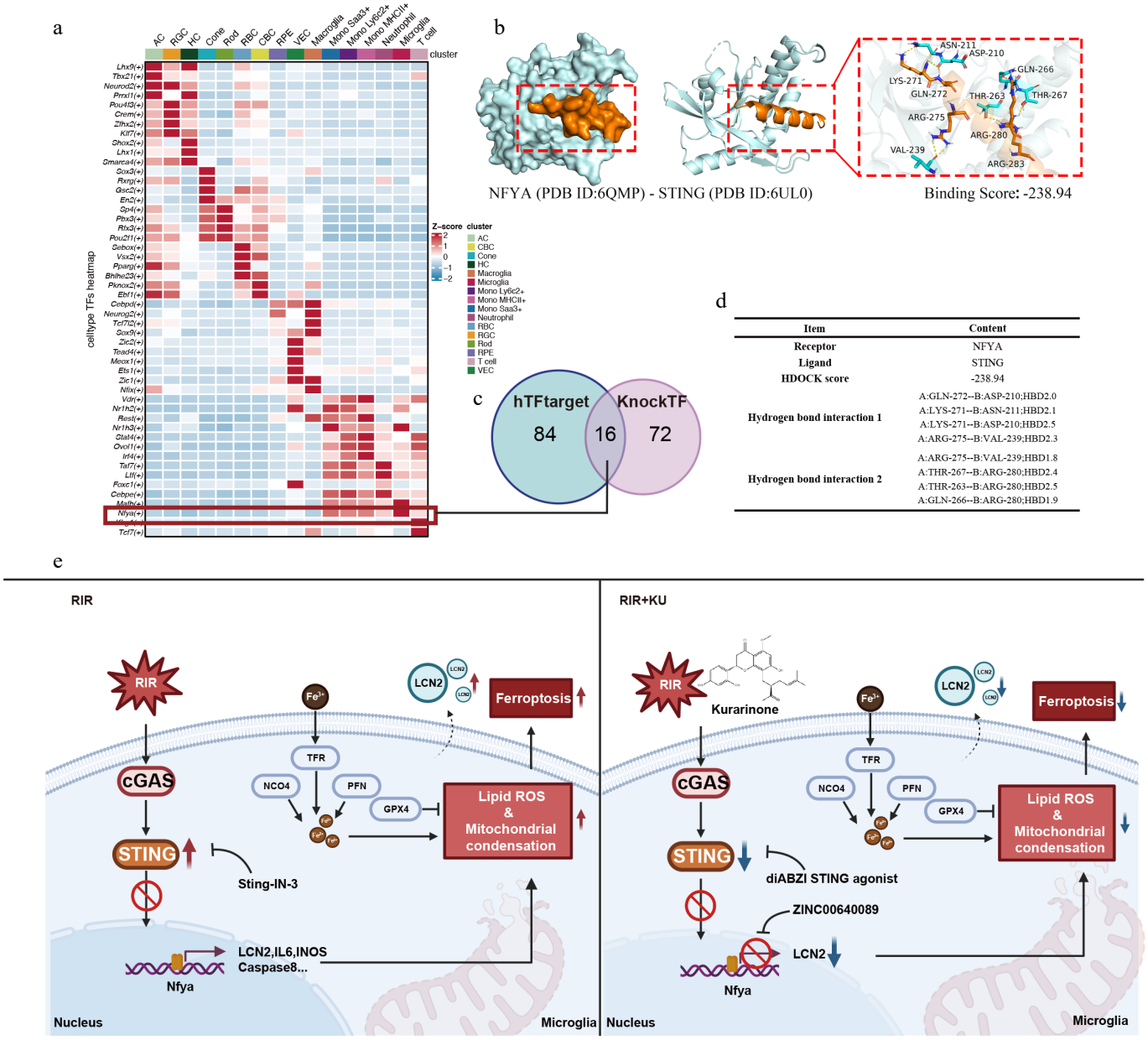

Fig. 7 NFYA is implicated as a potential STING-downstream transcription factor for LCN2 regulation. (a) The heatmap displays expression levels of major differentially expressed transcription factors in different cell types. (b) The STING protein is shown in blue, the NFYA protein in orange, and hydrogen bonding interactions are represented by yellow dashed lines. (c) Venn diagrams were used to identify overlapping transcription factors from major databases for screening upstream regulators of LCN2. (d) Specific hydrogen bonds and binding energies obtained from the molecular docking are shown in (b). (e) Schematic illustrating how KU ameliorates glaucoma-related RIR injury through the suppression of ferroptosis-induced lipid peroxidation. During RIR, disrupted iron metabolism and elevated reactive oxygen species production trigger glial cell activation. Pretreatment with KU inhibits the activity of the STING pathway and suppresses the expression of its downstream effector, LCN2, consequently mitigating ferroptosis. Ultimately, this mechanism protects retinal ganglion cells by attenuating the overall neuroinflammatory state in the retina.

suppression. KU treatment markedly reduced LCN2 and TFR levels while increasing FPN expression, resulting in decreased cellular uptake of transferrin-bound iron and enhanced iron efflux, ultimately attenuating ferroptosis. Notably, administration of a specific LCN2 inhibitor recapitulated these protective effects. These findings reveal that, under KU regulation, LCN2 influences cellular iron homeostasis through direct iron transport and by modulating iron storage stability, thereby providing new molecular insights into KU-mediated suppression of ferroptosis.

By examining the potential involvement of STING-related signaling and LCN2-associated iron dysregulation in microglial ferroptosis, this study provides preliminary evidence that KU may have neuroprotective effects in acute glaucoma. Single-cell RNA sequencing generated hypotheses about the interplay between iron metabolism and neuroinflammation that require targeted validation. Several limitations should be acknowledged. First, chemical modulators of STING and LCN2 may lack the specificity and precision of genetic approaches. Future investigations using CRISPR/Cas9-mediated gene knockout or conditional transgenic models could more rigorously evaluate the causal roles of these pathways. Second, the study primarily focused on microglia and may not fully capture the broader neuroprotective spectrum of KU, including its

potential effects on RGCs. Co-culture systems or *in vivo* lineage-tracing analyses could provide further insight into microglia-RGC crosstalk. Finally, validating KU in chronic or pressure-induced glaucoma models would clarify its translational relevance.

Ethical statements

This study protocol was approved by the Animal Care and Ethics Committee of Guangdong Provincial People's Hospital (No. KY2025-1314-01, Jan 4, 2026). The research followed the 'Replacement, Reduction, and Refinement' principles to minimize harm to animals.

Author contributions

The authors confirm their contributions to the paper as follows: study conception and design: Shi Y, Su W, Yu H; data analysis and interpretion: Shi Y, Zhang N, Liao Y; data curation and process: Zhuo Y, Pan Y, Ma C; writing the manuscript: Shi Y, Zhang N; details checking, formatting revision, and handling formatting proofreading tasks such as citation insertion: Luo Y, Zang S, Dong X, Yang C, Wang Y, Cheng Z; study supervision, providing funding and resources: Huang Z, Su W, and Yu H; All authors revised the paper, reviewed the results and approved the final version of the manuscript.

Data availability

Data generated during this study have been deposited in the Genome Sequence Archive in the BIG Data Center, Beijing Institute of Genomics (BIG, https://ngdc.cncb.ac.cn/gsa), Chinese Academy of Sciences, under the Project Accession No. PRJCA047349.

Acknowledgements

This work was supported by National Natural Science Foundation of China (U24A20707), the JSIEC Supporting Fund (26-015).

Conflict of interest

The authors declare that they have no conflict of interest.

Supplementary information accompanies this paper online at: https://doi.org/10.48130/vns-0026-0046.

Dates

Received 5 October 2026; Revised 20 October 2026; Accepted 24 October 2026; Published online 30 October 2026

References

[1] Asrani SG, McGlumphy EJ, Al-Aswad LA, Chaya CJ, Lin S, et al. 2024. The relationship between intraocular pressure and glaucoma: an evolving concept. *Progress in Retinal and Eye Research* 103:101303

[2] Jayaram H, Kolko M, Friedman DS, Gazzard G. 2023. Glaucoma: now and beyond. *The Lancet* 402(10414):1788–1801

[3] Agha RA, Mathew G, Rashid R, Kerwan A, Al-Jabir A, et al. 2025. Transparency in the reporting of artificial intelligence–the TITAN guideline. *Premier Journal of Science* 10:100082

[4] Bou Ghanem GO, Wareham LK, Calkins DJ. 2024. Addressing neurodegeneration in glaucoma: mechanisms, challenges, and treatments. *Progress in Retinal and Eye Research* 100:101261

[5] Hakim A, Guido B, Narsineni L, Chen DW, Foldvari M. 2023. Gene therapy strategies for glaucoma from IOP reduction to retinal neuroprotection: progress towards non-viral systems. *Advanced Drug Delivery Reviews* 196:114781

[6] Jiang B, Yao Q, Yuan X, Liu G, Lu P. 2024. Burden of blindness and vision loss in China over the past 30 years: findings and predictions based on the Global Burden of Disease Study 2019. *The British Journal of Ophthalmology* 108(6):889–896

[7] Sun X, Zhou J, Zeng X, Jiang Y. 2025. Relationship between chemokine in aqueous humor and primary glaucoma: a meta-analysis. *American Journal of Ophthalmology* 273:1–12

[8] Si Z, Fan Y, Wang M, Zhao J, Zhang Y, et al. 2025. The role of RGC degeneration in the pathogenesis of glaucoma. *International Journal of Biological Sciences* 21(1):211–232

[9] Xu Z, Ma Y, Li J, Zhuang J, Liu Y, et al. 2025. Microglial phagocytosis involves hyperoxia-induced vessel regression in the neonatal retina. *Visual Neuroscience* 42:e004

[10] Zeng H, Chen B, Geng X, Zuo X, Wang Z, et al. 2026. GB1107 attenuates microglia-mediated neuroinflammation by targeting Galectin-3 in retinal ischemia–reperfusion injury. *Visual Neuroscience* 43:e009

[11] Lin Y, Xu J, Huang Q, Heng X, Yang Z, et al. 2025. Unraveling the role of microglial activation and immune regulation in glaucomatous neurodegeneration: insights into its dynamic interactions with retinal cells. *Visual Neuroscience* 42:e011

[12] Guo J, Chen X, Wu M, Wang D, Zhao Y, et al. 2024. Traditional Chinese medicine FYTF-919 (Zhongfeng Xingnao oral prescription) for the treatment of acute intracerebral haemorrhage: a multicentre, randomised, placebo-controlled, double-blind, clinical trial. *Lancet* 404(10468):2187–2196

[13] Bjørklund G, Antonyak H, Lysiuk R, Dzhura N, Gurgas L, et al. 2026. The role of traditional Chinese medicine in COVID-19 treatment: integrating ancient wisdom with modern medicine. *Current Medicinal Chemistry* 33(2):255–283

[14] Yin Q, Xiang L, Han X, Zhang Y, Lyu R, et al. 2025. The evolutionary advantage of artemisinin production by *Artemisia annua*. *Trends in Plant Science* 30(2):213–226

[15] Sun CP, Zhou JJ, Yu ZL, Huo XK, Zhang J, et al. 2022. Kurarinone alleviated Parkinson's disease *via* stabilization of epoxyeicosatrienoic acids in animal model. *Proceedings of the National Academy of Sciences of the United States of America* 119(9):e2118818119

[16] Pan Y, Deng B, Wang T, Zhou Z, Wang J, et al. 2025. Kurarinone ameliorates intestinal mucosal inflammation *via* regulating T cell immunity. *Frontiers in Immunology* 16:1587479

[17] Kushwaha PP, Shuaib M, Prajapati KS, Singh AK, Kulharia M, et al. 2023. Abstract 4955: Kurarinone, a natural Notch signaling inhibitor and modulator of breast cancer stemness. *Cancer Research* 83(7_Supplement):4955

[18] Li Z, Lin M, Li Y, Shao J, Huang R, et al. 2022. Total flavonoids of *Sophora flavescens* and kurarinone ameliorated ulcerative colitis by regulating Th17/Treg cell homeostasis. *Journal of Ethnopharmacology* 297:115500

[19] Gu C, Liu Y, Lv J, Zhang C, Huang Z, et al. 2025. Kurarinone regulates Th17/Treg balance and ameliorates autoimmune uveitis *via* Rac1 inhibition. *Journal of Advanced Research* 69:381–398

[20] Lu QB, Sun HT, Zhou K, Su JB, Meng XY, et al. 2025. Therapeutic targeting of Decr1 ameliorates cardiomyopathy by suppressing mitochondrial fatty acid oxidation in diabetic mice. *Journal of Cachexia, Sarcopenia and Muscle* 16(2):e13761

[21] Yu H. 2025. Advancing visual neuroscience: expanding boundaries from bench to bedside. *Visual Neuroscience* 42:e001

[22] Kilkenny C, Browne WJ, Cuthill IC, Emerson M, Altman DG. 2012. Improving bioscience research reporting: the ARRIVE guidelines for reporting animal research. *Osteoarthritis and Cartilage* 20(4):256–260

[23] Shi Y, Lin J, Wu Y, Xu S, Zhang N, et al. 2026. Spatial multi-omics unveils sphingolipid metabolic reprogramming within the retinal pathological niche. *iMeta* 5(4):e70163

[24] Shi Y, Liu Y, Wu C, Liu X, Hu W, et al. 2023. N, N-Dimethyl-3β-hydroxycholenamide attenuates neuronal death and retinal inflammation in retinal ischemia/reperfusion injury by inhibiting Ninjurin 1. *Journal of Neuroinflammation* 20(1):91

https://doi.org/10.48130/vns-0026-0046

[25] Saelens W, Cannoodt R, Todorov H, Saeys Y. 2019. A comparison of single-cell trajectory inference methods. *Nature Biotechnology* 37(5):547−554

[26] Li Y, Yuwen W, Liu X, Li Z, Lin B, et al. 2022. Single-cell RNA sequencing reveals a landscape and targeted treatment of ferroptosis in retinal ischemia/reperfusion injury. *Journal of Neuroinflammation* 19(1):261

[27] Huang Y, Xia X, Li D, Lyu Y, Zhou P, et al. 2026. Qingguang'An II decoction attenuates retinal ganglion cell pyroptosis in glaucoma *via* inhibition of the TRPV4/NF-κB signaling pathway. *Journal of Ethnopharmacology* 355(Pt A):120576

[28] Yang J, Zhang M, Song Q, Li S, Zhao X, et al. 2021. Integrating network pharmacological and experimental models to investigate the therapeutic effects of baicalein in glaucoma. *Chinese Medicine* 16(1):124

[29] Hu L, Xu Y, Meng H. 2022. Development and evaluation of puerarin loaded-albumin nanoparticles thermoresponsive *in situ* gel for ophthalmic delivery. *Drug Design, Development and Therapy* 16:3315−3326

[30] Kumari S, Dhapola R, Sharma P, Paidlewar M, Vellingiri B, et al. 2025. Unravelling neuronal death mechanisms: the role of cytokines and chemokines in immune imbalance in Alzheimer's disease progression. *Ageing Research Reviews* 112:102883

[31] Yang K, Tang Z, Xing C, Yan N. 2024. STING signaling in the brain: molecular threats, signaling activities, and therapeutic challenges. *Neuron* 112(4):539−557

[32] Huang Y, Liu B, Sinha SC, Amin S, Gan L. 2023. Mechanism and therapeutic potential of targeting cGAS-STING signaling in neurological disorders. *Molecular Neurodegeneration* 18(1):79

[33] Zhang J, Xu Q, Sun G. 2025. Lipocalin-2 promotes NSCLC progression by activating the JAK2/STAT3 signaling pathway. *Journal of Translational Medicine* 23:419

[34] Adler O, Zait Y, Cohen N, Blazquez R, Doron H, et al. 2023. Reciprocal interactions between innate immune cells and astrocytes facilitate neuroinflammation and brain metastasis *via* lipocalin-2. *Nature Cancer* 4(3):401−418

[35] Song X, Xu S, Song D, Wang J, Bai B, et al. 2025. TGFB1/CXCL5 axis regulation by LCN2 overexpression: a promising strategy to inhibit colorectal cancer metastasis and enhance prognosis. *Frontiers in Immunology* 16:1548635

[36] Li Z, Zhang J, Yin J, Ma W, Liao H, et al. 2025. Targeting MYOF suppresses pancreatic ductal adenocarcinoma progression by inhibiting ILF3-LCN2 signaling through disrupting OTUB1-mediated deubiquitination of ILF3. *Redox Biology* 84:103665

[37] Xu J, Wang B, Liu Q, Guo S, Chen C, et al. 2025. MVP-LCN2 axis triggers evasion of ferroptosis to drive hepatocarcinogenesis and sorafenib resistance. *Drug Resistance Updates* 81:101246

[38] Deng Y, Lu L, Zhu D, Zhang H, Fu Y, et al. 2024. MafG/MYH9-LCN2 axis promotes liver fibrosis through inhibiting ferroptosis of hepatic stellate cells. *Cell Death and Differentiation* 31(9):1127−1139

[39] Yao F, Deng Y, Zhao Y, Mei Y, Zhang Y, et al. 2021. A targetable LIFR-NF-κB-LCN2 axis controls liver tumorigenesis and vulnerability to ferroptosis. *Nature Communications* 12(1):7333

[40] Liu J, Song X, Kuang F, Zhang Q, Xie Y, et al. 2021. NUPR1 is a critical repressor of ferroptosis. *Nature Communications* 12:647

[41] Hao X, Shi H, Wu D, Liang R, Zhao T, et al. 2026. LCN2-ACOD1 signalling affects the post-injury regeneration of skeletal muscle through mediating ferroptosis. *Cell Proliferation* 59(4):e70130

[42] Wang Y, Zhang Y, Gao M, Chen Z, Lu J, et al. 2024. Lipocalin-2 promotes CKD vascular calcification by aggravating VSMCs ferroptosis through NCOA4/FTH1-mediated ferritinophagy. *Cell Death & Disease* 15(11):865

[43] Gu L, Chen H, Geng R, Sun M, Shi Q, et al. 2024. Single-cell and spatial transcriptomics reveals ferroptosis as the most enriched programmed cell death process in hemorrhage stroke-induced oligodendrocyte-mediated white matter injury. *International Journal of Biological Sciences* 20(10):3842−3862

[44] Wang D, Li X, Jiao D, Cai Y, Qian L, et al. 2023. LCN2 secreted by tissue-infiltrating neutrophils induces the ferroptosis and wasting of adipose and muscle tissues in lung cancer *Cachexia*. *Journal of Hematology & Oncology* 16:30

[45] Zhang Y, Wei Y, Han X, Shi L, Yu H, et al. 2025. *Faecalibacterium prausnitzii* prevents age-related heart failure by suppressing ferroptosis in cardiomyocytes through butyrate-mediated LCN2 regulation. *Gut Microbes* 17(1):2505119

[46] Liu X, Li Y, Chen S, Yang J, Jing J, et al. 2023. Dihydromyricetin attenuates intracerebral hemorrhage by reversing the effect of LCN2 *via* the system Xc- pathway. *Phytomedicine* 115:154756

[47] Zhou Z, Zhang P, Ya D, Liu J, Xu Y, et al. 2024. Withaferin A protects against epilepsy by promoting LCN2-mediated astrocyte polarization to stopping neuronal ferroptosis. *Phytomedicine* 132:155892

[48] Gupta U, Ghosh S, Wallace CT, Shang P, Xin Y, et al. 2023. Increased LCN2 (lipocalin 2) in the RPE decreases autophagy and activates inflammasome-ferroptosis processes in a mouse model of dry AMD. *Autophagy* 19(1):92−111

Copyright: © 2026 by the author(s). Published by Maximum Academic Press, Fayetteville, GA. This article is an open access article distributed under Creative Commons Attribution License (CC BY 4.0), visit https://creativecommons.org/licenses/by/4.0/.